Pereira, L., Saraiva, I. H., Oliveira, A. S. F., Soares, C. M., Louro, R. O., & Frazão, C. (2017). Molecular structure of FoxE, the putative iron oxidase of Rhodobacter ferrooxidans SW2. *Biochimica et Biophysica Acta (BBA) - Bioenergetics*, *1858*(10), 847-853. https://doi.org/10.1016/j.bbabio.2017.07.002

Molecular structure of FoxE, the putative iron oxidase of *Rhodobacter ferrooxidans* SW2

Luis Pereira[a,1], Ivo H. Saraiva[a,1], A. Sofia F. Oliveira[a], Cláudio M. Soares[a], Ricardo O. Louro[a,2], Carlos Frazão[a,2]

[a] Instituto de Tecnologia Química e Biológica António Xavier, ITQB NOVA, Av. da República, 2780-157 Oeiras, Portugal.

[1] LP and IHS contributed equally to this work.

[2] To whom correspondence may be addressed. Email: louro@itqb.unl.pt or frazao@itqb.unl.pt

Abstract

The ancient metabolism of photoferrotrophy is likely to have played a key role in the biogeochemical cycle of iron on Early Earth leading to the deposition of Banded Iron Formations prior to the emergence of oxygenic photosynthesis. Extant organisms still performing this metabolism provide a convenient window to peer into its molecular mechanisms. Here we report the molecular structure of FoxE, the putative terminal iron oxidase of *Rhodobacter ferrooxidans* SW2. This protein is organized as a trimer with two hemes and a disulfide bridge per monomer. The distance between hemes, their solvent exposure and the surface electrostatics ensure a controlled electron transfer rate. They also guarantee segregation between electron capture from ferrous iron and electron release to downstream acceptors, which do not favor the precipitation of ferric iron. Combined with the functional characterization of this protein, the structure reveals how iron oxidation can be performed in the periplasmic space of this Gram-negative bacterium at circumneutral pH, while minimizing the risk of mineral precipitation and cell encrustation.

Research Highlights

- Crystal structure of phototrophic *Rhodobacter ferrooxidans* SW2 iron oxidase
- Provides a view of the molecular mechanism of photoferrotrophy
- A three-fold NCS oxidase, whose monomers harbor pairs of homologous cytochromes-c
- The 3D structure suggests an intricate duplication of an ancestral gene
- The structure reveals how iron terminal oxidation may safely occur in SW2 periplasm

Keywords: photoferrotrophy, cytochrome, electron transfer, crystallography, surface electrostatics

1. Introduction.

Since its emergence more than 3.8 billion years ago, life has co-evolved together with Earth through the biogeochemical cycling of elements, in the lithosphere, hydrosphere and atmosphere [1-3]. The current interpretation of the geological record indicates that oceans in the Archean and Proterozoic periods were predominantly ferruginous [4], and therefore suitable for biological anaerobic iron oxidation. This reaction is thermodynamically feasible at circumneutral pH and leads to the formation of ferric (hydr)oxides. These are insoluble at neutral pH, and indeed during the Proterozoic era, massive geological structures known as Banded Iron Formations were deposited. Banded Iron Formations are composed of alternating layers of iron rich minerals, typically iron oxides, and layers that are iron poor. For the period prior to the emergence of oxygenic photosynthesis at about 2.4 billion years ago,

two general mechanisms for the deposition of BIFs are proposed: the UV-photooxidation model and the anoxygenic-Fe(II) oxidizing phototrophic. However, experiments simulating the Precambrian ocean chemistry argue for a minor contribution of the UV-photooxidation model and favor the model postulating that these structures were mainly originated by bacteria performing photoferrotrophy [5]. This is an ancient photosynthetic metabolism characterized by the utilization of ferrous iron as electron source for photosynthesis: $4Fe^{2+} + CO_2 + 11H_2O + hv \leftrightarrows [CH_2O] + 4Fe(OH)_3 + 8H^+$ [6, 7]. Oxidation of soluble ferrous iron by those organisms was feasible because, under neutral conditions the reduction potential of the iron(III)/iron(II) couple is typically lower than that of their phototrophic reaction center.

The study of contemporary photoferrotrophs, which retain functional similarities to the earliest photosynthetic organisms [8], provides a window into this key biogeochemical process that took place during the so called Earth's middle age. This period predated the Great oxidation event (GOE) that lead to oxygenation of the atmosphere and the oceans and ultimately to the emergence of multicellular life. One of the first isolated photoferrotrophs was the freshwater purple bacterium *Rhodobacter ferrooxidans* SW2 (SW2). In this Gram-negative bacterium, a specific operon, *foxEYZ*, was shown to be involved in iron oxidation [9]. The composition of this operon lead to the proposal that the molecular mechanism for photoferrotrophy in SW2 reflects pathways that evolved prior to the GOE [10]. Its study is, therefore, relevant for exploring processes that likely mimic those taking place during Earth's middle age. The first gene of this operon, *foxE*, encodes a periplasmatic *c*-type diheme cytochrome predicted to be the iron oxidoreductase. The functional characterization of this protein showed that it is thermodynamically and kinetically able to perform iron oxidation at rates similar to other known iron oxidizing proteins [11-13]. However, the end-product of this reaction is a solid-phase mineral and although some microorganisms do undergo encrustation, this is not the case of SW2. In the case of SW2, ferric deposits are associated with extracellular polymeric substances [14]. This occurs despite the fact that the presumed terminal iron oxidoreductase FoxE is likely located in the periplasm of SW2 [12]. In this aspect, SW2 follows one of the two major strategies employed by non-encrusting neutrophilic iron oxidizers for organizing the iron oxidizing redox chains. Whereas lithotrophic organisms such as *Sideroxydans lithotrophicus* and phototrophic organisms such as *Rhodopseudomonas palustris* TIE-1 use decaheme cytochromes exposed at the cell surface to perform iron oxidation [11, 15], other lithotrophs such as *Mariprofundus ferrooxydans* and phototrophs such as SW2 perform this reaction in the periplasmic space [9, 16]. In the former case the porin-cytochrome complex at the cell surface, performs ferrous iron oxidation outside of the cell reducing the danger of precipitation in the cell, whereas in the latter case the mechanism for excreting ferric iron to the cell exterior remains to be identified. In fact it has been proposed that dissimilatory iron oxidation

may have evolved independently in multiple occasions, both before and after the GOE and therefore is supported by different kinds of redox proteins and metabolic pathway organization [10]. A structural characterization of the iron oxidase of *Sideroxydans lithotrophicus* representing the strategy of iron oxidation at the cell surface was already reported [11] but no such information currently exist to reveal how this process can be safely performed in the periplasmic space. The lack of homology between the primary sequence of FoxE and that of other known terminal ferrous oxidases, its proposed similarity to enzymes presumably operating before the GOE, and its relevance for one of the two broad strategies for biological neutrophilic iron oxidation, begs for the functional characterization of this protein to be complemented by a detailed structural analysis. This is presented here.

2. Materials and Methods

2.1. FoxE production and purification

The *E. coli* strain JCB7123 containing the plasmid pEC86, which expresses the cytochrome *c* maturation operon, was used. Expression of *foxE* was achieved using the plasmid pUX19. Cells were grown in 3 L of LB medium in 5 L conical flasks for 24h at 30°C and 140 rpm. After cell harvesting, the periplasm was extracted by resuspending the cells in extraction solution (0.5 *M* sucrose, 0.2 *M* TrisHCl, 0.5 m*M* EDTA, 100 $mg.L^{-1}$ lysozyme, pH 8) followed by a 30 min incubation at 0°C. The resulting spheroblasts were pelleted and the supernatant, containing the periplasm, was cleared by ultracentrifugation at 138000 g for 30 min. The periplasmic fraction was dialyzed twice against 20 m*M* TrisHCl pH 7.6 and loaded into a DEAE ionic exchange chromatography column. Bound proteins were eluted with 20 m*M* TrisHCl 1 *M* NaCl pH 7.6. Fractions containing FoxE were pooled, washed with 5 m*M* phosphate buffer pH 7 in an ultrafiltration cell with a 30 kDa cut-off and loaded into a hydroxylapatite chromatography column. Pure FoxE was eluted with 50 m*M* phosphate buffer pH 7 [12].

2.2. FoxE crystallization, diffraction data collection and processing

FoxE was previously crystallized at 293 K as trigonal crystals and highly redundant diffraction data, measured at long wavelength 1.73925 Å, were collected up to 2.44 Å resolution [17]. Meanwhile, tetragonal crystals were obtained at 277 K in identical crystallization conditions, 2 µL sitting drops of equal volumes of protein solution, 15 $mg.mL^{-1}$ of FoxE in 5 m*M* potassium phosphate buffer pH 7, and precipitant solution, 1.2 *M* sodium/potassium phosphate pH 7 and 50 m*M* copper chloride. Diffraction data up to 2.67 Å resolution were collected in station ID14-4 of the European Synchrotron Radiation Facility (ESRF), Grenoble, France. Data were processed with XDS [18] and 5 % of the reflections in bins of thin resolution shells were flagged for Rfree monitoring purposes using Phenix.refine [19, 20]. Crystal solvent contents

[21] were estimated with Matthews Probability Calculator [22]. Crystallographic parameters and diffraction data statistics are presented in Table 1.

2.3. Crystallographic phasing, structures refinement and analysis

We reported previously the phase problem solution of FoxE trigonal crystal by single wavelength anomalous diffraction (SAD) [17]. Meanwhile, we used Phenix.AutoBuild [19, 23] for automatic FoxE sequence re-build followed by Phenix.AutoMR [19, 24] for molecular replacement (MR) of the tetragonal crystal form. Log likelihood anomalous maps were calculated with Phaser in CCP4 [24, 25]. Coot [26] modeling sessions of crystals structures led to structural models improvement and completion, including solvent components whose chemical nature (P, S, Fe and Cu) was corroborated with their anomalous signal. Modeling sessions alternated with Phenix.refine [19, 20] refinement runs that included non crystallographic symmetry (NCS) restraints in addition to those from standard stereochemistry libraries [27]. TLSMD (http://skuld.bmsc.washington.edu/~tlsmd) [28] was used to determine domains of translation, libration and screw motions (TLS) for TLS refinement. The stereochemistry of the final models was assessed with MolProbity [29]. Secondary structure was assigned with PROMOTIF[30]. 3D superposition of poly-peptide chains was performed with MODELLER [31]. A PDB search of proteins with structure similar to FoxE was produced with Dali Server[32]. Solvent accessible surface areas were calculated with AREAIMOL [25, 33] and surface electrostatic distributions with APBS [34], where sets of atomic radii and partial charges were taken from GROMOS 54A7 force field [35] for all the residues, except for the heme centers, where quantum chemical calculations were used to derive the partial charges (see Table S4). Images of structural models, electron density maps and electrostatic potential distribution surfaces were prepared with COOT [26] and PYMOL [36]. GEOMCALC from CCP4 [25] suite was used to calculate geometric relationships between hemes. The FoxE trigonal and tetragonal crystal structures coordinates and structure factors were deposited in the PDB with accession codes 5MAB and 5MVO, respectively.

3. Results and discussion.

3.1. Intricate duplication of ancestral FoxE gene.

FoxE is a 259 residues all alpha di-heme protein. A 38 residues long protruding N-terminus is structured in two anti-parallel helices that provide stabilization to FoxE oligomerization (see section 3.2.). It is followed by a 221 residues hydrophobic core that harbors two hemes-*c* with methionine sulfur atoms as heme-iron distal ligands. The polypeptide chain binds covalently to heme I via residues Cys 59, Cys 62 and His 63, but then proceeds towards heme II, where it binds via residues Met 116, Cys 169, Cys 172 and His 173, and finally the chain returns back to heme I, where it binds via Met 230. Therefore the two hemes show different orders in

the covalent attachment of their hemes-*c* binding motifs, with CxxCH of heme I preceding the axial methionine ligand, whereas in heme II is the axial methionine that precedes CxxCH.

A visual examination of FoxE hydrophobic core hinted for the presence of local two-fold symmetry relating the peptide chains around the two hemes, and therefore two models of FoxE were superposed: in a first step hemes I and II of one model were manually overlaid with hemes II and I of the second model, respectively, and in a second step the Cα atoms of the resulting superpositioned chains were 3D fitted with program MODELLER[31]. It became clear that the two hemes are surrounded by sets of homologous alpha-helices and 3_{10}-helical segments (Figs. 1 and S1): heme I is surrounded by chain segments 39-114 and 229-259 with juxtapositioned termini forming a composite chain of 107 residues that overlays admirably with chain segment 115-228 (114 residues) that wraps heme II. Their 3D fit led to 101 C-alpha atoms superposition with 1.3 Å rmsd (up to 3.5 Å distance cut-off), and corresponded to sequences identity of 34%. However, as the hemes-*c* linkers, CxxCH and methionine, have inverted sequence orders, the superposition of the poly-peptide chains implied a "re-ordering" of the sequence around heme I (residues 229-259 *followed by* 39-114) with the carboxylic group of residue 259 vicinal to the amino group of residue 39, in positions homologous to residues 145 and 147, respectively, of the continuous chain harboring heme II (Figs. 1 and S1). Although residue 259 is not linked to residue 39, a disulfide bridge between cysteines 80 and 258 provided an ancillary covalent bond between the chain segments, which stabilizes the C-terminus conformation.

(2-column fitting image)

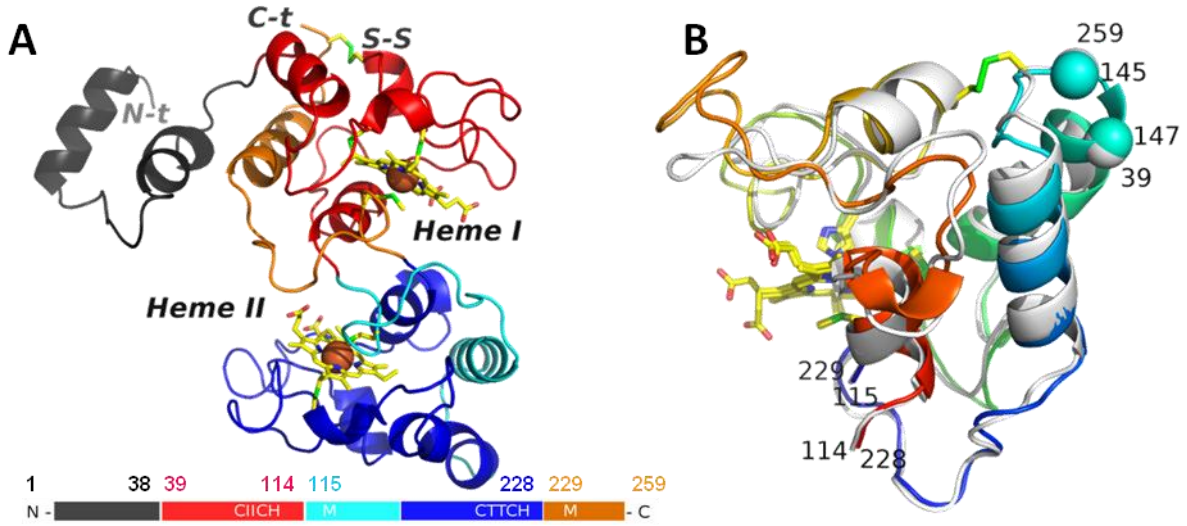

Figure 1. FoxE monomer presents a whole-α structure nesting two hemes**. A.** Cartoon representation (top) of FoxE structure with N-terminus in black, the polypeptide around heme I in red and orange, and around heme II in cyan and blue. Labels of colours along FoxE peptide sequence (bottom) include heme binding motifs CHxxH and methionines, as well as the numbers of the residues limiting structural motifs. Heme atoms and disulfide bonds are represented as sticks coloured in yellow (carbon), blue (nitrogen), red (oxygen), green (sulphur), and with iron atoms as orange spheres. **B.** Cartoon of the superposition of the two polypeptide folding motifs wrapping heme I (in grey) and heme II (colours of residues 114 to 227 ramping from blue to red). Disulfide bonds, heme atoms, and iron ligands are represented as sticks.

The sequence layout of FoxE hints for an insertion of the heme II wrapping motif (Fig. 1A bottom, in cyan and blue) into the peptide surrounding heme I (Fig. 1A bottom, in red and orange), while the 3D resemblances between both hemes-*c* harboring motifs suggest that FoxE might have derived from a gene duplication event of an ancestral heme-*c* binding motif. The inverted orders in peptide linkage required a further transposition between chain segments. Interestingly, such a sequence layout is also present in the di-heme cytochrome CcoP, one of the chains from cbb_3 cytochrome oxidase C of *Pseudomonas stutzeri*, PDB ID: 5DJQ [37]. Noteworthy, FoxE and CcoP 3D structures share no resemblance in their chain paths, which results in very different hemes relative localization, *e.g.* FoxE hemes are near parallel to each other (see section 3.4) and stay 16 Å apart, while CcoP hemes are near perpendicular to each other and within hydrogen bonding distances.

(1.5-column fitting image)

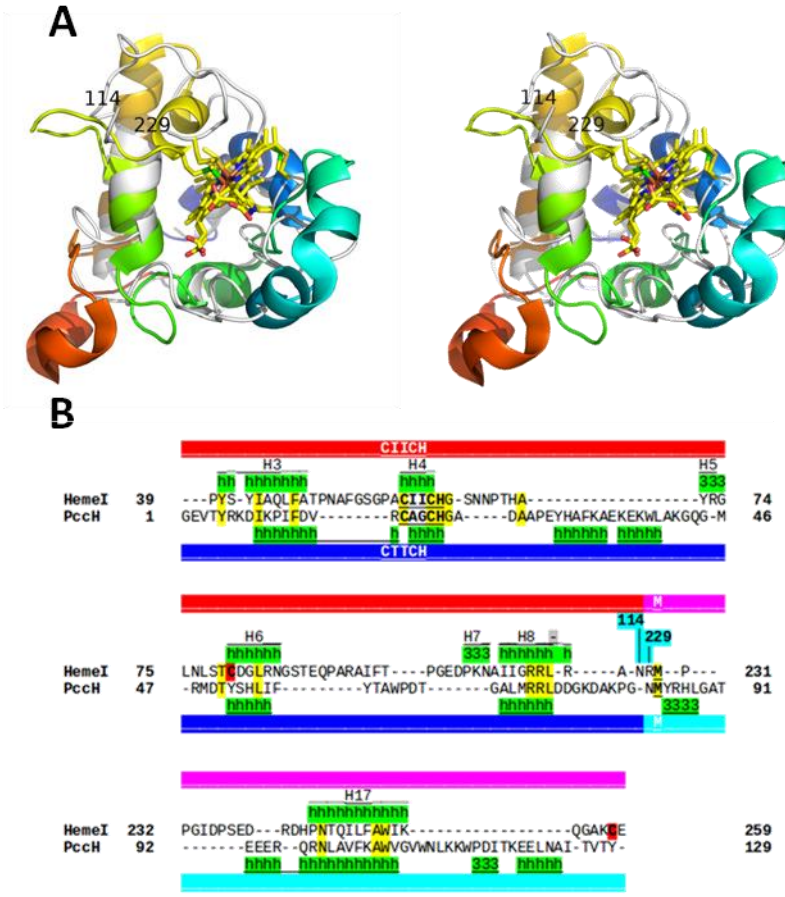

Figure 2. Superposition of FoxE heme I wrapping poly-peptide, residues 39-114 and 229-259, against PccH from *Geobacter sulfurreducens* cytochrome-*c* [38]. **A.** Cartoon representation in cross eyes stereo-view with FoxE in grey and PccH in colour ramping from blue (N-terminus) to red (C-terminus). Hemes and their ligands are represented in sticks, the two inner peptide termini of FoxE heme I wrapping peptide are highlighted with their residue numbers. **B.** Sequences, aligned according with residues 3D superposition, are highlighted in yellow for residues conserved in both cytochromes, in red for cysteine residues involved in FoxE disulfide bridge, in cyan for the inner termini of FoxE composite peptide surrounding heme I, and underscored and bold for residues in heme binding motifs. Green highlights secondary structure elements, where "h" indicates α-helices and "3" indicates 3_{10}-helices. The two structures share a set of five homologous helical structures.

A search in the PDB for protein structures similar to FoxE, using the Dali server[32], led to several hits. Their visual inspection showed that only the best qualified hit (with a Z score 4.7) presented features similar to those of FoxE, in contrast with other three hits (with Z scores within 2.9-2.8). The highest hit corresponded to the recently determined structure of PccH from *Geobacter sulfurreducens*, a mono-heme cytochrome-*c* with 129 residues, PDB ID: 4RLR [38]. Its heme binding topology corresponds to that of FoxE heme I binding poly-peptide, and their 3D fit led to 2x64 C-alpha atoms superposition with 1.6 Å rmsd and 27%

identity (Fig. 2). Given that *Geobacter* can reduce metallic minerals, it was interesting to find two unrelated micro-organisms showing the same cytochrome-*c* fold, which suggests an evolutionary advantage derived for this fold in the interaction of bacteria with insoluble substrates or products.

(2-column fitting image)

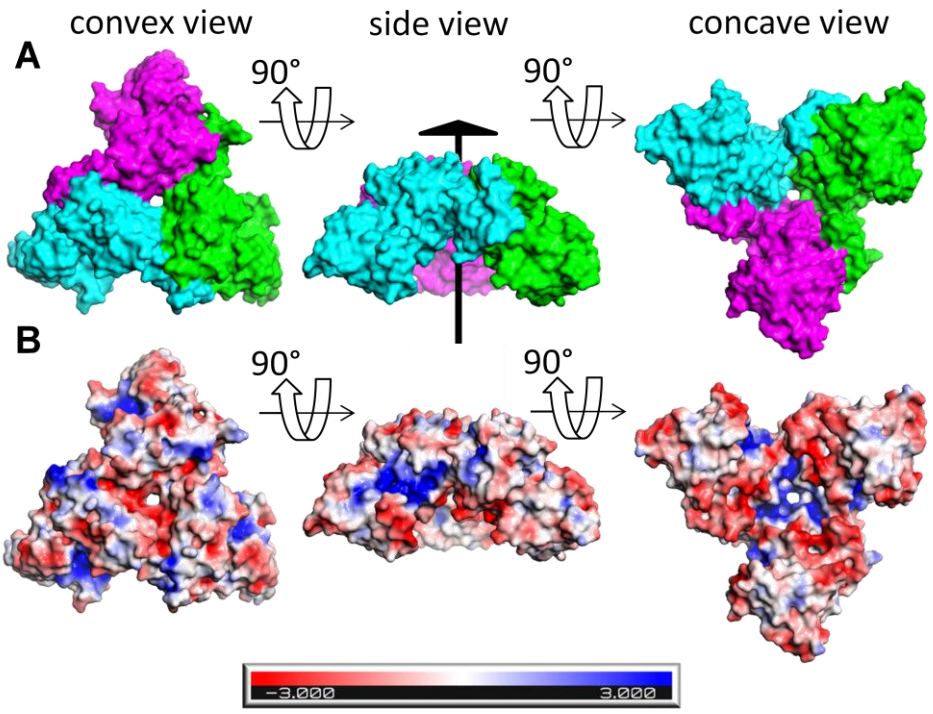

Figure 3. FoxE trimer. **A.** Views of FoxE trimer molecular surface, coloured differently for each monomer, with the NCS three-fold rotation axis displayed in the side-view image. **B.** Similar views to previous panel but with the surface mapped with electrostatic potential distribution. The potential varies between -3 and +3 KT/e, as shown in the colours bar (middle below), with red and blue representing negative and positive potentials, respectively.

3.2. FoxE oligomerization

The two FoxE crystals are built of similar asymmetric units (*a.u.*'s) of three monomers, assembled around a non-crystallographic symmetry (NCS) three-fold rotation axis (Fig. 3 and S2). Their N-termini, up to residue 38, protrude out of FoxE globular fold and produce neighboring contacts, 4 salt-bridges and 20 hydrogen-bonds, while occluding *ca.* 990 Å^2 (7%) of closest neighbor solvent accessible surface (SAS). As each monomer is flanked by two neighbors, FoxE trimerization eliminates 3x2x990 Å^2 (14%) of otherwise SAS. The SAS

occluded area upon oligomerization is more than twice that involved in inter-trimers crystal packing contacts, thus strongly indicating that the quaternary structure observed in both crystal forms is also present in solution, which is in agreement with previous DLS data of FoxE [12].The trimer envelope is reminiscent of a trigonal bowl, with a outer convex and a inner concave face, both displaying deep grooves, *e.g.* at inter-monomers contact borders, and a central hole crossed by the three-fold NCS axis.

3.3. A structural disulfide bridge

In addition to the four cysteine residues from heme-*c* binding motifs, FoxE includes two other cysteines at positions 80 and 258 (Fig. 1A). Both crystals show contiguous electron density between the SG atoms of these two cysteines (not shown), thus revealing a disulfide bond. Disulfide bonds may play either structural or functional roles. Structural disulfide bonds stabilize protein folds, while functional disulfide bonds mediate thiol-disulfide redox reactions. These occur in either disulfide substrate catalytic proteins or in disulfide allosteric proteins, where they trigger conformational changes upon disulfide break and/or formation [39]. The ultimate criterion to assign structural *versus* functional roles to a disulfide bond is its reduction potential: while in structural disulfide proteins the reduction potential can be as low as -470 mV, potentials within -330 to -95 mV have been reported in thiol–disulfide oxidoreductases [40]. Given that the hemes of FoxE have reduction potentials in the range of 200-300 mV, and the whole redox chain from FoxE to the phototrophic reaction center operates at positive potentials [12], these disulfide bridges are unlikely to have a physiological redox role. Further support for a structural role comes from data collected during the functional characterization of FoxE. The NMR spectrum of FoxE underwent reversible transitions upon reaction of the protein with the mild reducer sodium ascorbate, which is unable to reduce disulfide bridges. However, reduction with the strong reducer sodium dithionite, which is capable of reducing disulfide bridges, led to irreversible spectral changes in the signals of the high potential heme [12]. The distance of the cystine to heme I is half of that to heme II (15 *vs.* 30 Å, Fig. 4A). Given the likelihood that the treatment with sodium dithionite disrupted the disulfide bridge and affected irreversibly the protein fold in its vicinity, the high potential heme can be tentatively assigned to heme I that is the closest to the disulfide bridge.

3.4. Heme architecture and reduction potentials

In each monomer of FoxE the heme planes lie nearly parallel to each other (35° angle) but their ring directions diverge by about 90°.

(2-column fitting image)

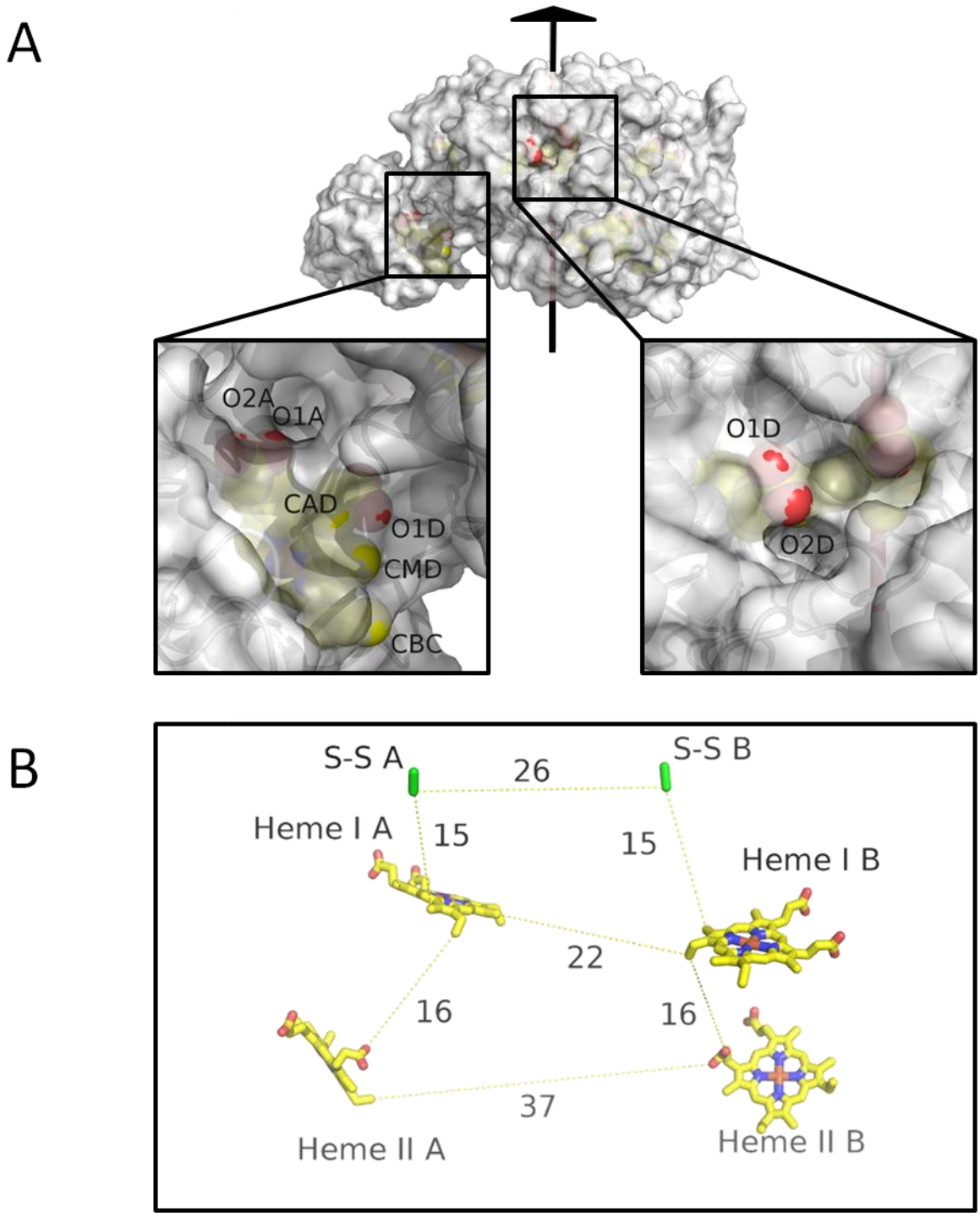

Figure 4. Redox centers of FoxE. **A**. Transparent representation of the FoxE trimer molecular surface superposed with the van der Waals surfaces of heme atoms (coloured in yellow and red for carbons and oxygens atoms, respectively) and showing the three-fold non-crystallographic symmetry axis (top). Two zoomed views highlight the solvent accessible atoms of heme I on the convex surface (bottom right) and of heme II on the concave surface (bottom left). **B.** Distances between hemes and cystines. View of the spatial distribution of FoxE hemes-*c* and cystine S-S bonds for chains A and B (chain C omitted for clarity) with indication of their shortest distances in Ångstrom.

Heme I is located close to the convex surface of the trimer bowl, at *ca.*15 Å from the three-fold NCS axis that runs through the bowl hole. It exposes to the solvent *ca.* 5% (40-55 $Å^2$, interval among the three chains) of its SAS area. Heme II lies near to the concave surface, close to the edge of the trimer bowl at 22 Å distance from the NCS axis. It exposes to the solvent *ca.* 10% (70-85 $Å^2$) of its SAS (Fig. 4A, Table S1). Both hemes expose their propionic groups to the solvent, but in contrast to heme II, heme I is involved in intra-oligomer contacts, which hinder the access to the solvent of its C and D edges. The observed difference in solvent exposure between the hemes is therefore a result of the oligomer architecture. The two hemes are imbedded in homologous poly-peptide chain motifs and expose similarly their carboxylic groups to the solvent, but they show different reduction potentials [12]. Heme I, with its relative lower solvent exposure [41] and slightly higher ratio of basic/acidic neighboring residues at closer distances (Table S2) seems to correspond to FoxE high potential heme [12], because its ferric state is less stabilized relative to heme II, and therefore more prone to be reduced. The hemes are separated by a distance of 16 Å within each monomer, and by 22 Å for the closest hemes between neighboring monomers (Fig. 4B). This observation confirms the predictions of inter-heme distances made on the basis of the slow intramolecular electron exchange between the high potential and low potential hemes deduced from NMR data of FoxE [12]. It also shows that iron oxidation is unlikely to rely on electron transfer between hemes located in different monomers, which according to the Moser-Dutton ruler is expected to be about four orders of magnitude slower than electron transfer between hemes in the same monomer [42].

3.5. The design of the FoxE trimer hinders Fe^{3+} precipitation

The calculated electrostatic potential of FoxE was mapped on its molecular surface producing patches of positive and negative regions, both in the concave and convex sides of the trimer bowl. The convex surface shows a slight predominance of positive regions, whereas the concave surface shows a slight predominance of negative ones (Fig. 3B) Interestingly, a bowl shaped structure was also reported for the soluble fragment of MamP, the iron-oxidoreductase leading to the formation of magnetite nano-particles in magnetotatic bacteria (PDB ID: 4JJ0) [13]. However, there are marked differences from FoxE. Whereas MamP forms a crucible with strong negative electrostatic surface (Fig. S4), the bottom of the bowl formed by the FoxE trimer has positive electrostatics and a 5 Å diameter hole. Furthermore, whereas the propionates of the hemes closest to the crucible bottom in the soluble fragment of MamP are pointing inwards, in FoxE heme I that is closest to the bowl bottom is exposed to the outside, keeping the distance between heme I in different subunits larger than 20A (Fig. 4B). These differences are likely related to the different physiological role of the two proteins.

Whereas MamP is involved in an iron oxidation pathway leading to a controlled growth of iron nano-particles inside bacterial cells, FoxE is involved in a dissimilatory iron oxidation pathway that needs to avoid mineral precipitation in the periplasmic space. The iron would be oxidized by heme II which is exposed to the concave surface and the resulting iron hydroxide would be well spread given the distance of 37 Å between hemes II of different monomers. It is of great importance for anoxygenic phototrophs to successfully prevent mineral precipitation in the periplasm: presence of the minerals would reduce the exchange of nutrients and metabolic products with the environment, and would reduce the amount of light reaching the phototrophic reaction center [43].

3.6. A protein for the safe iron oxidation in the periplasm at circumneutral pH

The molecular structure of FoxE the putative terminal iron oxidase of the photoferrotroph *Rhodobacter ferrooxidans* SW2 hints at the way this process takes place in a controlled fashion within the periplasmic space of this Gram-negative bacterium. The large distance between hemes from different subunits of the trimer, and the fact that iron oxidation extracts a single electron per iron atom strongly suggests that the oligomerization does not serve a functional role. Its purpose is most likely to ensure the segregation of the iron oxidation reaction from the electron transfer reaction to the partner mediating the delivery of electrons to the cyclic electron transfer chain. Hemes I and II are exposed to the convex and the concave surface of FoxE, respectively, and have small SAS areas. This suggests that electron extraction from Fe(II) and egress from the protein is exquisitely controlled. Heme II appears to be responsible for iron oxidation in the concave surface of the FoxE trimer. Before it is able to initiate anew round of oxidation it needs to transfer the electron to heme I.The unusual large distance to heme I likely serves the purpose of ensuring that this transfer proceeds slow enough to allow diffusion away of the ferric hydroxide product, before the new round of iron oxidation can take place. The slow intramolecular electron transfer, together with the fact that FoxE is a soluble protein and therefore its activity does not give rise to a fixed location of high ferric hydroxide concentration, serves to minimize the risk of ferric iron precipitation in the periplasmic space.

The electron captured by heme II is delivered to heme I which is exposed to the convex surface of FoxE. The concave and convex surfaces of the trimer bowl show electrostatic bias, with the concave surface predominantly negatively charged whereas the convex surface is predominantly positively charged. The organization of the *fox* operon suggests that the redox partner of FoxE is FoxY, a pyrroloquinoline quinone binding protein. The predicted isoelectric point of FoxY, after removing the signal peptide for translocation into the periplasm, is 5.34. This means that the protein is negatively charged at neutral pH and likely prefers to bind to

the convex surface of FoxE. After being reduced by heme I of FoxE, FoxY can deliver the electrons to the cyclic electron transfer pathway.

4. Conclusions.

In the ferruginous oceans of Earth middle age, photoferrotrophy is likely to have powered the bulk of primary production of organic matter, a role only lost with the advent of oxygenic photosynthesis [44].This transition is unlikely to have been abrupt and there are extant analogues of communities where oxygenic and anoxygenic photosynthesis co-exist [45]. Iron oxidation at circumneutral pH is a metabolic activity that requires exquisite control to avoid the spontaneous precipitation of solid phase minerals that would be lethal to the cells. The structure of FoxE, the iron oxidoreductase supporting the photoferrotrophic metabolism of extant *Rhodobacter ferrooxidans* SW2, reveals how this can be accomplished by a protein that is soluble in the periplasmic space of this Gram-negative bacterium. The bowl shaped structure of the trimer with distinct electrostatic bias on the concave and convex surface segregates the ferrous iron oxidation reaction from electron transfer to the redox partner. The large distance between the hemes within the structure slows down intramolecular electron transfer minimizing the risk of product accumulation and ferric hydroxide precipitation, while the soluble nature of FoxE means that a fixed hot-spot of ferric hydroxide production does not exist in the periplasm. Indeed, SW2 shows precipitation of iron minerals only away from the cells and is associated with extracellular polymeric substances that appear to direct the process of converting poorly crystalline iron hydroxide into minerals such as goethite [14]. This solution for the iron precipitation problem appears to have evolved prior to the solution developed by other organisms involving porin cytochrome supercomplexes at the cell surface [10]. Although there are currently no genomes available for marine photoferrotrophs, there are strong similarities between the anaerobic freshwater bacterium SW2 and the marine *Rhodovulum iodosum* with respect to the mineralogical nature of the iron precipitates and their association to extracellular polymeric substances [14, 46]. These observations argue for the relevance of the current study to illuminate the molecular details of processes that may have contributed to the precipitation of vast amounts of iron from the ferruginous Archaean oceans in the form of Banded Iron Formations.

Acknowledgements: This work was financially supported by Fundação para a Ciência e Tecnologia (FCT) through grants SFRH/BPD/84404/2012(IHS) and SFRH/BPD/76621/2011. This work was further supported by MOSTMICRO (Lisboa-01-0145-FEDER-007660). We also would like to thank to the staff of ESRF beamlines ID23 and ID14 for assistance during synchrotron data collection. The authors are grateful to Prof. Dianne K. Newman for very helpful discussions and suggestions.

Table 1. Crystallographic parameters and structures refinement statistics

ESRF beamline	ID23-1	ID14-4
Space group [a]	$P3_121$	$P4_32_12$
Wavelength (Å)	1.73925	0.97959
Resolution (Å) [b]	57.83-2.44 (2.54-2.44)	49.85-2.67 (2.77-2.67)
Unit-cell parameters (Å)	*a*=*b*=112.77, *c*=143.54	*a*=*b*=16.85, *c*=119.13
No. of reflections	1293342	433362
No. of unique reflections	38526 (3591)	38119 (2166)
Multiplicity	32.3 (6.3)	11.4 (10.2)
$\langle I \rangle / \langle \sigma(I) \rangle$	28.3 (1.9)	19.1 (2.8)
Rsym	13.6 (70.7)	8.3 (78.4)
Rmeas	13.6 (70.7)	8.7 (82.4)
Rpim	2.2 (25.1	2.5(15.6)
Data completeness (%)	96.1 (77.1)	99.2 (99.8)
Solvent contents (%)	59	46
Wilson B factor (Å^2)	56	67
Refinement		
No. protein molecules in *a.u.*	3	3
No. of residues per chain (total)	259, 259, 257 (775)	251, 259, 258 (769)
No. of solvent waters	101	44
No. of phosphate ions	7	6
No. of Cu sites	1	2
Rwork	0.1641	0.181
Rfree	0.2097	0.217
Rfactor	0.1702	0.179
<*adp*>s of protein by chains (Å^2)	53, 54, 56	101, 66, 65
<*adp*> s of hemes I/II by chains (Å^2)	36/44, 44/46, 42/48	66/122, 53/54, 52/54
adp of Cu sites by chains (Å^2)	--, 76, --	--, 87, 121
<*adp*>s of solvent waters (Å^2)	45	54
<*adp*>s of solvent phosphates (Å^2)	103	102
Bonds rmsd (Å^2)	0.020	0.013
Angles rmsd (°)	1.4	1.5
Ramachandran regions: distribution of favoured and disallowed residues (%)	97.4, 0.13	96.4, 1.05

Notes:
[a] Trigonal and tetragonal crystals were grown at 298 and 277 K, respectively.
[b] Values within parentheses correspond to highest resolution shells.

References.

[1] L.E. Dietrich, M.M. Tice, D.K. Newman, The co-evolution of life and Earth, Curr Biol, 16 (2006) R395-400.
[2] J.F. Kasting, J.L. Siefert, Life and the evolution of Earth's atmosphere, Science, 296 (2002) 1066-1068.
[3] A.P. Nutman, V.C. Bennett, C.R.L. Friend, M.J. Van Kranendonk, A.R. Chivas, Rapid emergence of life shown by discovery of 3,700-million-year-old microbial structures, Nature, 537 (2016) 535–538.
[4] T.W. Lyons, C.T. Reinhard, N.J. Planavsky, The rise of oxygen in Earth's early ocean and atmosphere, Nature, 506 (2014) 307-315.
[5] A. Kappler, C. Pasquero, K.O. Konhauser, Deposition of banded iron formations by anoxygenic phototrophic Fe(II)-oxidizing bacteria, Geology, 33 (2005) 865-868.
[6] L.J. Bird, V. Bonnefoy, D.K. Newman, Bioenergetic challenges of microbial iron metabolisms, Trends Microbiol, 19 (2011) 330-340.
[7] F. Widdel, S. Schnell, S. Heising, A. Ehrenreich, B. Assmus, B. Schink, Ferrous iron oxidation by anoxygenic phototrophic bacteria, Nature, 362 (1993) 834-836.
[8] J. Xiong, W.M. Fischer, K. Inoue, M. Nakahara, C.E. Bauer, Molecular evidence for the early evolution of photosynthesis, Science, 289 (2000) 1724-1730.
[9] L.R. Croal, Y. Jiao, D.K. Newman, The fox operon from Rhodobacter strain SW2 promotes phototrophic Fe(II) oxidation in Rhodobacter capsulatus SB1003, J Bacteriol, 189 (2007) 1774-1782.
[10] M. Ilbert, V. Bonnefoy, Insight into the evolution of the iron oxidation pathways, Biochim Biophys Acta, 1827 (2013) 161-175.
[11] J. Liu, Z. Wang, S.M. Belchik, M.J. Edwards, C. Liu, D.W. Kennedy, E.D. Merkley, M.S. Lipton, J.N. Butt, D.J. Richardson, J.M. Zachar, J.K. Fredrickson, K.M. Rosso, L. Shi, Identification and characterization of MtoA: a decaheme c-type cytochrome of the neutrophilic Fe(II)-oxidizing bacterium Sideroxydans lithotrophicus ES-1, Frontiers in Microbiology, 3 (2012) 1-11.
[12] I.H. Saraiva, D.K. Newman, R.O. Louro, Functional characterization of the FoxE iron oxidoreductase from the photoferrotroph Rhodobacter ferrooxidans SW2, J Biol Chem, 287 (2012) 25541-25548.
[13] M.I. Siponen, P. Legrand, M. Widdrat, S.R. Jones, W.J. Zhang, M.C. Chang, D. Faivre, P. Arnoux, D. Pignol, Structural insight into magnetochrome-mediated magnetite biomineralization, Nature, 502 (2013) 681-684.
[14] J. Miot, K. Benzerara, M. Obst, A. Kappler, F. Hegler, S. Schadler, C. Bouchez, F. Guyot, G. Morin, Extracellular iron biomineralization by photoautotrophic iron-oxidizing bacteria, Applied and environmental microbiology, 75 (2009) 5586-5591.
[15] Y. Jiao, D.K. Newman, The pio operon is essential for phototrophic Fe(II) oxidation in Rhodopseudomonas palustris TIE-1, J Bacteriol, 189 (2007) 1765-1773.
[16] E. Singer, D. Emerson, E.A. Webb, R.A. Barco, J.G. Kuenen, W.C. Nelson, C.S. Chan, L.R. Comolli, S. Ferriera, J. Johnson, J.F. Heidelberg, K.J. Edwards,

Mariprofundus ferrooxydans PV-1 the first genome of a marine Fe(II) oxidizing Zetaproteobacterium, PloS one, 6 (2011) e25386.
[17] L. Pereira, I.H. Saraiva, R. Coelho, D.K. Newman, R.O. Louro, C. Frazao, Crystallization and preliminary crystallographic studies of FoxE from Rhodobacter ferrooxidans SW2, an Fe(II) oxidoreductase involved in photoferrotrophy, Acta Crystallogr Sect F Struct Biol Cryst Commun, 68 (2012) 1106-1108.
[18] W. Kabsch, XDS, Acta Crystallographica Section D, 66 (2010) 125-132.
[19] P.D. Adams, P.V. Afonine, G. Bunkoczi, V.B. Chen, I.W. Davis, N. Echols, J.J. Headd, L.W. Hung, G.J. Kapral, R.W. Grosse-Kunstleve, A.J. McCoy, N.W. Moriarty, R. Oeffner, R.J. Read, D.C. Richardson, J.S. Richardson, T.C. Terwilliger, P.H. Zwart, PHENIX: a comprehensive Python-based system for macromolecular structure solution, Acta Crystallogr D Biol Crystallogr, 66 (2010) 213-221.
[20] P.V. Afonine, R.W. Grosse-Kunstleve, N. Echols, J.J. Headd, N.W. Moriarty, M. Mustyakimov, T.C. Terwilliger, A. Urzhumtsev, P.H. Zwart, P.D. Adams, Towards automated crystallographic structure refinement with phenix.refine, Acta Crystallogr D Biol Crystallogr, 68 (2012) 352-367.
[21] B.W. Matthews, Solvent content of protein crystals, Journal of molecular biology, 33 (1968) 491-497.
[22] K.A. Kantardjieff, B. Rupp, Matthews coefficient probabilities: Improved estimates for unit cell contents of proteins, DNA, and protein-nucleic acid complex crystals, Protein science : a publication of the Protein Society, 12 (2003) 1865-1871.
[23] T.C. Terwilliger, R.W. Grosse-Kunstleve, P.V. Afonine, N.W. Moriarty, P.H. Zwart, L.W. Hung, R.J. Read, P.D. Adams, Iterative model building, structure refinement and density modification with the PHENIX AutoBuild wizard, Acta Crystallogr D Biol Crystallogr, 64 (2008) 61-69.
[24] A.J. McCoy, R.W. Grosse-Kunstleve, P.D. Adams, M.D. Winn, L.C. Storoni, R.J. Read, Phaser crystallographic software, J Appl Cryst, 40 (2007) 658-674.
[25] M.D. Winn, C.C. Ballard, K.D. Cowtan, E.J. Dodson, P. Emsley, P.R. Evans, R.M. Keegan, E.B. Krissinel, A.G. Leslie, A. McCoy, S.J. McNicholas, G.N. Murshudov, N.S. Pannu, E.A. Potterton, H.R. Powell, R.J. Read, A. Vagin, K.S. Wilson, Overview of the CCP4 suite and current developments, Acta Crystallogr D Biol Crystallogr, 67 (2011) 235-242.
[26] P. Emsley, B. Lohkamp, W.G. Scott, K. Cowtan, Features and development of Coot, Acta Crystallogr D Biol Crystallogr, 66 (2010) 486-501.
[27] R.A. Engh, R. Huber, Accurate bond and angle parameters for X-ray protein structure refinement, Acta Crystallogr A Found Crystallogr, 47 (1991) 392-400.
[28] J. Painter, E.A. Merritt, Optimal description of a protein structure in terms of multiple groups undergoing TLS motion, Acta Crystallogr D Biol Crystallogr, 62 (2006) 439-450.
[29] I.W. Davis, A. Leaver-Fay, V.B. Chen, J.N. Block, G.J. Kapral, X. Wang, L.W. Murray, W.B. Arendall, 3rd, J. Snoeyink, J.S. Richardson, D.C. Richardson, MolProbity: all-atom contacts and structure validation for proteins and nucleic acids, Nucleic acids research, 35 (2007) W375-383.
[30] E.G. Hutchinson, J.M. Thornton, PROMOTIF--a program to identify and analyze structural motifs in proteins, Protein science : a publication of the Protein Society, 5 (1996) 212-220.
[31] A. Sali, T.L. Blundell, Comparative protein modelling by satisfaction of spatial restraints, Journal of molecular biology, 234 (1993) 779-815.
[32] L. Holm, P. Rosenstrom, Dali server: conservation mapping in 3D, Nucleic acids research, 38 (2010) W545-549.

[33] B. Lee, F.M. Richards, The interpretation of protein structures: estimation of static accessibility, Journal of molecular biology, 55 (1971) 379-400.
[34] N.A. Baker, D. Sept, S. Joseph, M.J. Holst, J.A. McCammon, Electrostatics of nanosystems: application to microtubules and the ribosome, Proc Natl Acad Sci U S A, 98 (2001) 10037-10041.
[35] N. Schmid, A.P. Eichenberger, A. Choutko, S. Riniker, M. Winger, A.E. Mark, W.F. van Gunsteren, Definition and testing of the GROMOS force-field versions 54A7 and 54B7, European Biophysics Journal with Biophysics Letters, 40 (2011) 843-856.
[36] W.L. DeLano, The PyMOL Molecular Graphics System, 0.83 Ed., DeLano Scientific, San Carlos, CA, USA, 2002.
[37] S. Buschmann, E. Warkentin, H. Xie, J.D. Langer, U. Ermler, H. Michel, The structure of cbb3 cytochrome oxidase provides insights into proton pumping, Science, 329 (2010) 327-330.
[38] J.M. Dantas, L.M. Campelo, N.E.C. Duke, C.A. Salgueiro, P.R. Pokkuluri, The structure of PccH from Geobactersulfurreducens-a novel low reduction potential monoheme cytochrome essential for accepting electrons from an electrode, Febs Journal, 282 (2015) 2215-2231.
[39] B. Schmidt, L. Ho, P.J. Hogg, Allosteric disulfide bonds, Biochemistry, 45 (2006) 7429-7433.
[40] M.A. Wouters, S.W. Fan, N.L. Haworth, Disulfides as redox switches: from molecular mechanisms to functional significance, Antioxid Redox Signal, 12 (2010) 53-91.
[41] R.J. Kassner, A theoretical model for the effects of local nonpolar heme environments on the redox potentials in cytochromes, J Am Chem Soc, 95 (1973) 2674-2677.
[42] C.C. Moser, C.C. Page, P.L. Dutton, Darwin at the molecular scale: selection and variance in electron tunnelling proteins including cytochrome c oxidase, Philos Trans R Soc Lond B Biol Sci, 361 (2006) 1295-1305.
[43] F. Hegler, C. Schmidt, H. Schwarz, A. Kappler, Does a low-pH microenvironment around phototrophic Fe(II) -oxidizing bacteria prevent cell encrustation by Fe(III) minerals?, FEMS microbiology ecology, 74 (2010) 592-600.
[44] D.E. Canfield, M.T. Rosing, C. Bjerrum, Early anaerobic metabolisms, Philos Trans R Soc Lond B Biol Sci, 361 (2006) 1819-1834; discussion 1835-1816.
[45] B.B. Jorgensen, Y. Cohen, N.P. Revsbech, Transition from Anoxygenic to Oxygenic Photosynthesis in a Microcoleus chthonoplastes Cyanobacterial Mat, Applied and environmental microbiology, 51 (1986) 408-417.
[46] W. Wu, E.D. Swanner, L. Hao, F. Zeitvogel, M. Obst, Y. Pan, A. Kappler, Characterization of the physiology and cell-mineral interactions of the marine anoxygenic phototrophic Fe(II) oxidizer Rhodovulum iodosum--implications for Precambrian Fe(II) oxidation, FEMS microbiology ecology, 88 (2014) 503-515.